

Reconfigurable-Metasurface-Aided Multi-State Generalized Polarization-Space Modulation for Next-Generation Wireless Communications

John A. Hodge^{†1}, Kumar Vijay Mishra^{‡2}, Quang M. Nguyen^{‡3}, and Amir. I. Zaghoul^{†‡4}
[†]Bradley Department of Electrical and Computer Engineering, Virginia Tech, Blacksburg, VA 24061 USA
[‡]United States CCDC Army Research Laboratory, Adelphi, MD 20783 USA*

(Dated: March 24, 2021)

We propose a low-cost reconfigurable metasurface transmitter to implement generalized polarization-space modulation (GPSM) that has been proposed for next-generation wireless communications. Unlike conventional multiple-input multiple-output GPSM, our electromagnetically-compliant, reduced form-factor design using Barium-Strontium-Titanate film yields more than two polarization states. Full-wave simulations show our optimized design achieves 0.08-0.95 polarization conversion ratio with 5% bandwidth at 28 GHz and bit error rates comparable or better than conventional systems.

I. INTRODUCTION

In conventional wireless communications systems, the user messages are encoded by distinct complex vectors or codewords such as a quadrature amplitude modulation (QAM) constellation. Lately, demands[1] for high data rates in communications networks proposed for future fifth-generation (5G) and beyond are driving research in exploiting the indices of other transmission resources such as frequency subcarriers, antenna elements or subarrays (SAs), and temporal slots to allow encoding of additional information bits. This technique of *index modulation* [2, 3] (IM) has recently garnered significant attention because it offers improvements in data rates, spectral efficiency (SE), and energy efficiency (EE). For example, the indices of the transmit (Tx) antennas of a multiple-input multiple-output (MIMO) system [4] and the frequency subcarriers [3] are used for encoding in the basic IM forms known as spatial modulation (SM) and orthogonal frequency division multiplexing (OFDM), respectively.

Prior works on IM focus largely on using the spatial, temporal, and frequency indices. Recent works have introduced polarization IM (PoIM) [5], which employs a generalized polarization shift keying (PolarSK) modulation scheme for dual-polarization (DP) communications and leverages Tx polarization states as additional indices to achieve high SE. A further improvement in bit-error-rate (BER) was obtained by extending [6] the classical two-dimensional (2-D) polarization modulation (PM) constellation to 3-D by mapping symbols from a sphere to respective horizontal (H-) and vertical polarizations (V-pol). Here, the indices of both polarization states and phase of a radiated electromagnetic (EM) wave were used. Similarly, a DP spatial modulation (DP-SM) [7] considers the dimension of polarization to transmit additional information bits for correlated Rayleigh and Rician

fading channels under channel estimation errors; an additional information bit is mapped to a selected (vertical or horizontal) polarization [8].

Very recently, generalized polarization-space modulation (GPSM) [6] has been proposed as an extension of PolarSK for multiple-input multiple-output (MIMO) systems with a limited number of radio frequency (RF) chains [9]. It allows concurrent activation of multiple DP Tx antennas with one polarization state per antenna per time slot. The GPSM extends SM [4] through inclusion of polarization as an additional degree-of-freedom (DoF) and activating more than one antenna to increase SE. For example, if the transmit data bit is 0 (1), the V-pol (H-pol) state is selected. In the conventional PolarSK system, SE is increased by employing more than two polarization states, as in *slant polarization*, using a linear combination of the V- and H-pol states [5]. The PolarSK systems have only one DP transmit antenna so that the available DoF in the spatial domain remains unexploited. Note that the GPSM may be compared to other similar extensions of basic IMs such as generalized spatial modulation (GSM) [10] or generalized SSK (GSSK) [11].

The 5/6G MIMO communications are envisaged to use large arrays and, consequently, require multiple RF chains. To facilitate low-cost and reduced form-factor of such systems, reconfigurable metasurface (RMTS) [12] is currently being investigated for feasibility [12–15]. The RMTS is capable of controlling and manipulating EM waves through modified surface boundary conditions [16–18]. These surfaces are electrically thin and comprise an array of spatially-varying sub-wavelength scattering elements (or meta-atoms). Prior works demonstrate anisotropic MTS to manipulate EM wave polarization [19–22]. The RMTS performs signal processing and filtering operations through spatial and time modulation [23, 24]. In particular, the introduction of RMTS as a wireless technology has given rise to the concept of smart radio environments [25] that intelligently adapt to changing environments by overcoming signal attenuation from multi-path fading, blockages, and other uncontrollable interference.

* ¹jah70, ⁴amirz}@vt.edu, ²kumarvijay-mishra@uiowa.edu, ⁴quang.m.nguyen7.ctr@mail.mil

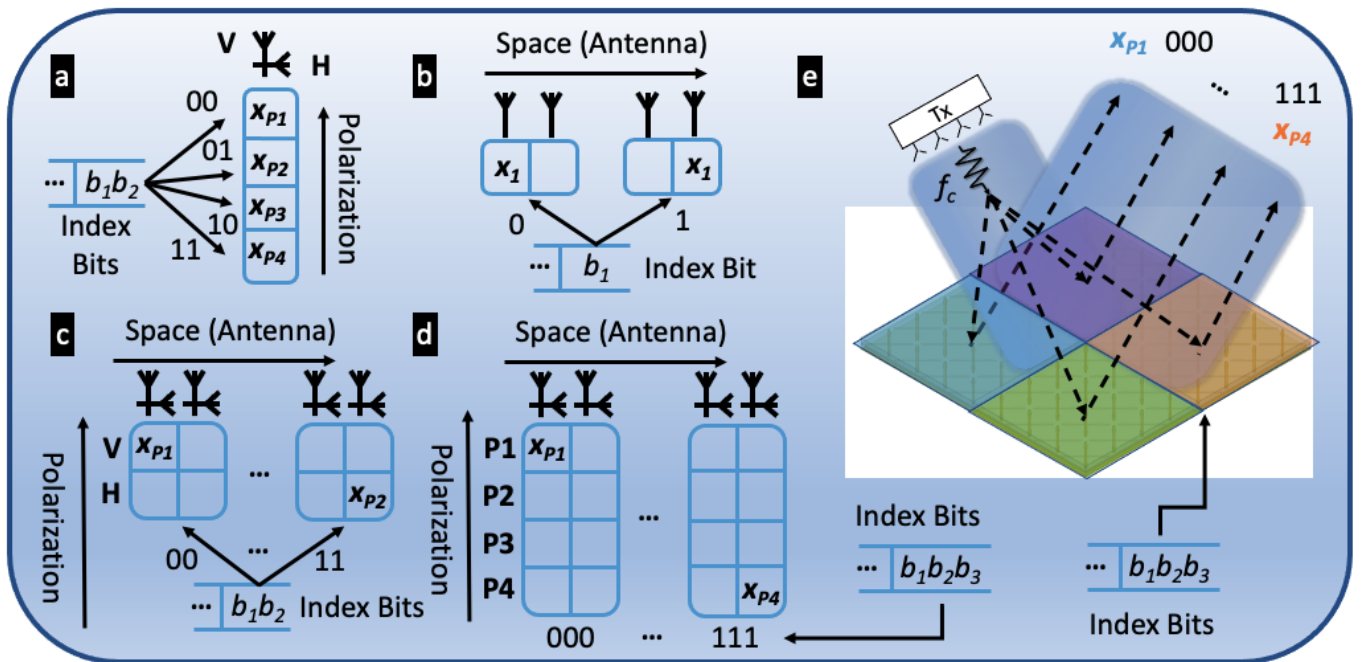


FIG. 1. Schematic of the transmit index mapping approaches for conventional (a) PolarSK [5] (single DP antenna with only polarization states used for mapping) (b) SM [4] (multiple antennas without any polarization diversity) (c) DP-SM [7] (only two polarizations per antenna) (d) GPSM [9] (multiple polarizations per antenna), and our proposed (e) RMTS-enhanced GPSM transmitter. The user message is given by the sequence of bits b_0, b_1, \dots . RMTS is illuminated with an incident carrier wave with a single polarization. The MTS inclusions are electrically tuned to reflect the modulated signal with the desired polarization state.

The RMTS applies customized transformations to radio waves based on the propagation channel and provides low-cost multi-function integrated antennas and transceivers [15]. The RMTS directly performs signal modulation on the antenna surface thereby avoiding a large number of costly and power-hungry independent RF chains and beamforming networks [13]. However, specific implementations and EM analyses of RMTS designs of IM systems remain relatively unexamined.

In this context, our prior works [12, 14] consider implementing RMTS for wireless communications through careful engineering of each meta-atom [26–29] to transform an incident EM wave into an arbitrarily tailored transmitted or reflected wavefront. Similar meta-atom elements are utilized to modify the radiation patterns of antennas through near-field parasitic coupling [30, 31]. The RMTS is designed to operate as beam-steering reflect-array [32, 33] or transmit-array antennas [33, 34], which may be polarization agnostic [32]. In [35], we showed RMTS implementations of frequency-domain IM (FD-IM) techniques, such as OFDM-IM. Recently, we introduced RMTS-aided media-based modulation [36] to improve the bit error rate (BER) using channel as a DoF.

In this paper, we introduce the RMTS implementation of GPSM to achieve a reduced form-factor that is optimized to provide maximum polarization tunability. Further, unlike the conventional DP phased array system of GPSM [9] that requires a MIMO Tx antenna

with multiple RF chains and produced only two polarization states, our proposed design requires only single RF feed source and yields more than two polarizations. This reduces the cost and RF complexity of the transceiver. We verify the polarization conversion performance using finite-element method (FEM) full-wave EM simulations, which are later used to provide realistic co-polarization and cross-polarization levels while evaluating BER at the receiver (Rx). Figure 1 compares our RMTS-assisted GPSM scheme with PolarSK, SM, DP-SM, and GPSM. Table I quantitatively summarizes these systems.

II. RMTS POLARIZER

Previous works on MTS-based polarization conversion [37–40] and reconfiguration [41] use varactor or PIN diodes as the tunable element [41–45]. In this paper, in place of a diode, we employ MTS with a tunable Barium Strontium Titanate (BST) substrate to achieve polarization modulation. The BST is a ferroelectric material with tunable capacitance that is suitable for RF components due to its producibility, low-cost, and high speed characteristics [46].

The polarization conversion principle of our RMTS polarizer design is as follows. The electric and magnetic resonant features of the unit cell allow tuning of the reflected signal between two orthogonal polarization states.

TABLE I. Comparison of the proposed method with the state-of-the-art

Modulation	Total Tx Antennas	Activated Tx Antennas	Polarization States (P)	Polarization Angles (K)	Data Rate ^a (R) (bits/s/Hz)	RF Chains (N_{RF})	Dynamic Radiation Patterns
PolarSK [5]	1	1	≥ 2	≥ 1	$\log_2(P)$	1	No
SM [4]	$N_T \geq 2$	$N_{\text{RF}} < N_T$	1	1	$\log_2(N_T) + \log_2(M)$	N_{RF}	No
DP-SM [7]	$N_T \geq 2$	$N_{\text{RF}} < N_T$	2	1	$\log_2(PN_TM)$	N_{RF}	No
GPSM [9]	$N_T \geq 2$	$N_{\text{RF}} < N_T$	≥ 2	≥ 1	$\lfloor \log_2 \left(\frac{N_T}{N_{\text{RF}}} \right) \rfloor + N_{\text{RF}} \lfloor \log_2(P) \rfloor$	N_{RF}	No
This paper	$N_T \geq 2$	$N_{\text{SA}} < N_T$	≥ 2	≥ 1	$\lfloor \log_2 \left(\frac{N_T}{N_{\text{SA}}} \right) \rfloor + N_{\text{SA}} \lfloor \log_2(P) \rfloor$	1	Yes

^a For various notations used here, we refer the reader to the supplement on GPSM signal model.

^b The function $\lfloor \cdot \rfloor$ yields the greatest integer smaller than or equal to the argument.

Dipoles [37] and v-shaped [38] resonators rotated 45 degrees relative to the electric (E) field of the incident wave \mathbf{E}^i are used to realize linear polarization conversion metasurfaces. The unit vectors for the Cartesian x -, y -, and z - axes are $\hat{\mathbf{x}} = \frac{\mathbf{x}}{|\mathbf{x}|}$, $\hat{\mathbf{y}} = \frac{\mathbf{y}}{|\mathbf{y}|}$, and $\hat{\mathbf{z}} = \frac{\mathbf{z}}{|\mathbf{z}|}$. The incident wave is

$$\mathbf{E}^i(z) = \hat{\mathbf{x}}E_0e^{-jk_zz}, \quad (1)$$

where $\hat{\mathbf{x}}$ is the unit vector in the x -direction, E_0 is the E -field magnitude in volts per meter (V/m) and k_z is the wavenumber for the wave propagating in the $-\hat{\mathbf{z}}$ direction. The E -field of the wave reflected by the MTS is decomposed into two orthogonal components u and v such that $\mathbf{E}_u = \mathbf{E}_x + \mathbf{E}_y$ and $\mathbf{E}_v = \mathbf{E}_y - \mathbf{E}_x$. Denote the four reflected polarization components by $r_{xx} = |\mathbf{E}_x^r|/|\mathbf{E}_x^i|$, $r_{xy} = |\mathbf{E}_x^r|/|\mathbf{E}_y^i|$, $r_{yx} = |\mathbf{E}_y^r|/|\mathbf{E}_x^i|$, and $r_{yy} = |\mathbf{E}_y^r|/|\mathbf{E}_y^i|$. The incident and reflected waves are \mathbf{E}^i and \mathbf{E}^r , respectively. The subscripts x and y indicate the $\hat{\mathbf{x}}$ and $\hat{\mathbf{y}}$ polarized components, respectively, of the field. The resultant reflected E -field (\mathbf{E}^r) is the vector sum of the components

$$\mathbf{E}^r = E_x^r\hat{\mathbf{x}} + E_y^r\hat{\mathbf{y}}. \quad (2)$$

The magnitudes of \mathbf{E}^i and \mathbf{E}^r are related by

$$\begin{bmatrix} |\mathbf{E}_x^r| \\ |\mathbf{E}_y^r| \end{bmatrix} = \begin{bmatrix} r_{xx} & r_{xy} \\ r_{yx} & r_{yy} \end{bmatrix} \begin{bmatrix} |\mathbf{E}_x^i| \\ |\mathbf{E}_y^i| \end{bmatrix}. \quad (3)$$

Define the linear-to-linear cross-polarization conversion ratio (PCR) of a y -polarized wave as

$$\text{PCR} = \frac{r_{xy}}{r_{yy} + r_{xy}}. \quad (4)$$

Given an incident y -polarized wave, the objective of RMTS polarizer is to create a tunable change of polarization states with a PCR between 0 and 1. This implies that the MTS polarizer controls the proportion of \mathbf{E}_t between the orthogonal x and y polarizations. We realize the polarization states for GPSM by controlling the PCR.

The effective impedance Z of the meta-atom is modeled using an effective RLC circuit as

$$Z = R_{\text{eff}} + j \left(\omega L_{\text{eff}} - \frac{1}{\omega C_{\text{eff}}} \right) = R_{\text{eff}} + jX, \quad (5)$$

where R_{eff} is the effective resistance, $\omega = 2\pi f$ is the angular frequency, f is the carrier frequency of the signal, L_{eff} is the effective inductance produced by current on the metallic strips, C_{eff} is the effective capacitance between metallic strips and the groundplane, and X is the reactance. The impedances of the orthogonal polarization components \mathbf{E}_x and \mathbf{E}_y are $Z_x = R_x + jX_x$ and $Z_y = R_y + jX_y$, respectively. To realize the RMTS polarizer, we choose a meta-atom geometry that provides tunable X_x and X_y values to produce orthogonal polarization responses. Our design using a tunable BST-loaded substrate changes the effective dielectric constant ϵ_r of the meta-atom substrate. The meta-atom's effective capacitance C_{eff} is a function of ϵ_r . Subsequently, the reactance relates to ϵ_r as $X \sim 1/(C_{\text{eff}}(\epsilon_r))$.

The BST-loaded substrate offers tunable permittivity ϵ_r by applying an external bias voltage v_b [46]. Using a BST thin film between two Duroid ($\epsilon_r = 2.3$) slabs, we create a tunable composite dielectric substrate with an effective $\epsilon_r(v_b)$ ranging from 3.0 – 5.0 [33]. By controlling ϵ_r , we also regulate C_{eff} and hence X for each polarization within tunable ranges. By adjusting the effective dielectric constant of the meta-atom substrate, we control the electric resonance of two orthogonal dipoles.

The response of the multilayer RMTS polarizer is theoretically understood using a multilayer dielectric slab model [47]. When an incident wave \mathbf{E}_y^i is reflected off the MTS, the scattering response for each polarization [37, 43] is obtained using a transfer matrix method (TMM). Using boundary conditions, the reflection r and transmission t coefficients of forward and backward propagating waves at each substrate interface are summed up to compute the total reflected electric field [40]. Each metallic structure layer is treated as a zero-thickness impedance sheet where the coefficients are obtained through numerical EM simulations. From this model, we gain an intuitive understanding of multilayer meta-atom function as a tunable polarizer.

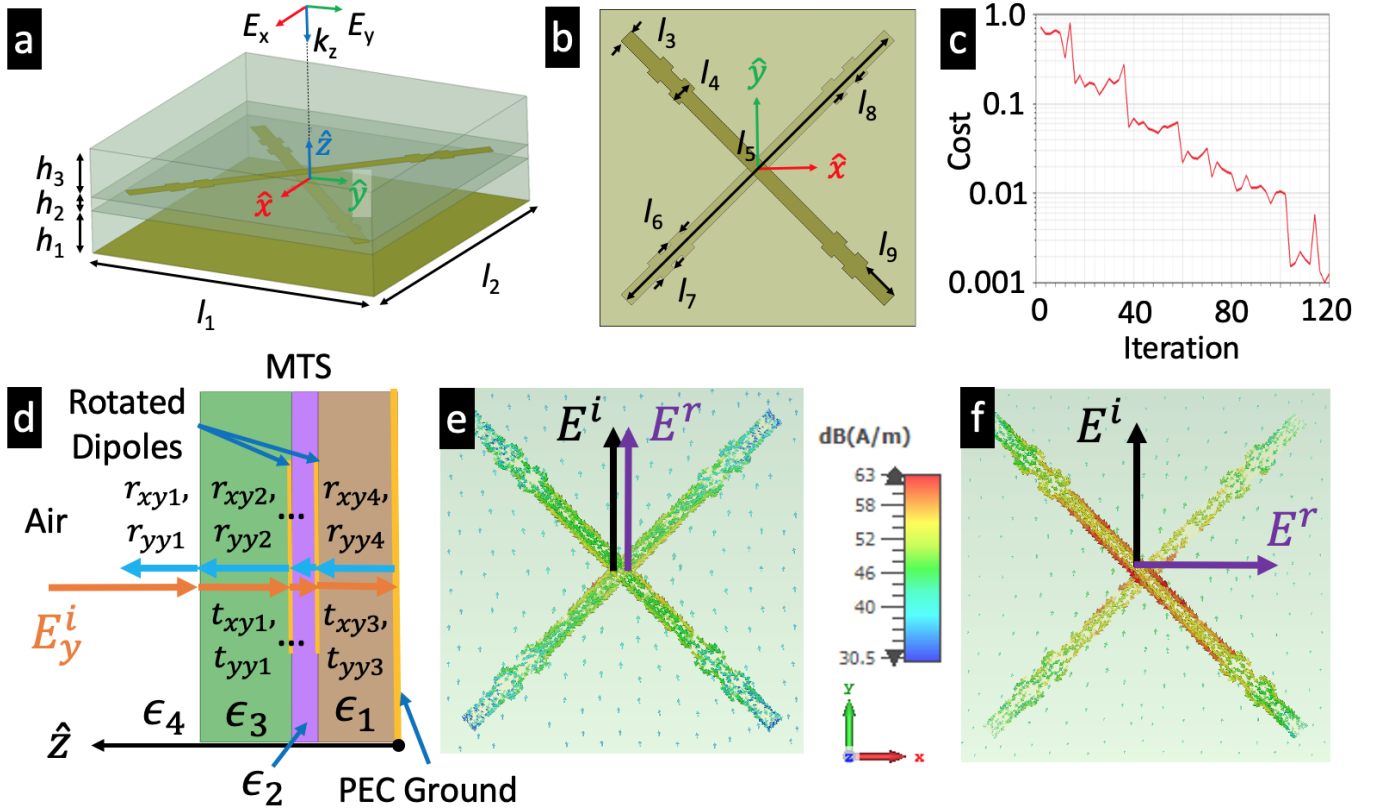


FIG. 2. (a) Isometric and (b) top-down views of our polarization conversion MTS unit-cell (meta-atom) with three layers including two orthogonal metallic dipoles. The Cartesian coordinates are shown in the XYZ space. The meta-atom dimensions are: $l_1 = l_2 = 2.046$ mm, $h_1 = 0.284$ mm, $h_2 = 0.093$ mm, $h_3 = 0.327$ mm, $l_3 = l_6 = l_7 = l_8 = 0.096$ mm, $l_4 = 0.146$ mm, $l_5 = 2.413$ mm, and $l_9 = 0.267$ mm. (c) Results of meta-atom optimization to maximize the tunable PCR range at $f = 28$ GHz. (d) Diagram of the material stack-up for the MTS in the \hat{z} -direction. The effective relative dielectric constants are $\epsilon_1 = 3.5$, $\epsilon_2 = 2.2$, ϵ_3 is tuned between 3.0 – 5.0, and $\epsilon_4 = 1.0$. For an incident wave \mathbf{E}_y^i , the transmission t and reflection r coefficients between each material layer are shown for the xyh and yyh polarization components (Eqn. 3) where h is the dielectric layer indices. (e-f) The surface current distribution and the polarization of the corresponding incident (\mathbf{E}^i) and reflected (\mathbf{E}^r) signals when (e) $\epsilon_3 = 3.0$ and (f) $\epsilon_3 = 5.0$.

III. REFLECTIVE POLARIZATION CONVERSION

We design a reflection-type MTS by incorporating constituent dielectric layer materials for controlling the polarization. The proposed design (Fig. 2) comprises three layers: the first consists of an I-shaped structure placed on top of a dielectric layer ($\epsilon_1 = 3.5$) with metal backing; the second is a dielectric spacer ($\epsilon_2 = 2.2$); and the third has an I-shaped structure placed on top of a constituent material and oriented 90° with respect to the first layer.

The physical dimensions of our meta-atom design are shown in Fig. 2a-b. We maximized the tunable PCR range of our RMTS at $f = 28$ GHz using ANSYS HFSS's gradient-based quasi-Newton optimizer. The orthogonal reflection coefficients $r_{xy}(\epsilon_3)$ and $r_{yy}(\epsilon_3)$ are functions of the tunable substrate ϵ_3 (Fig. 2e-f). We optimized the dimensions of our meta-atom using design variables h_1, h_2, h_3, l_4 , and l_5 (Fig. 2a-b) over 120 full-wave simulation iterations (Fig. 2c) to achieve the maximum tunable PCR

range subjected to the constraints

$$\begin{aligned} |r_{yy}(\epsilon_3 = 3.0)| &\geq 0.95 \\ |r_{xy}(\epsilon_3 = 3.0)| &\leq 0.05 \\ |r_{yy}(\epsilon_3 = 5.0)| &\leq 0.95 \\ |r_{xy}(\epsilon_3 = 5.0)| &\geq 0.05. \end{aligned}$$

The orthogonal metallic dipoles are separated by height of h_2 in the \hat{z} -direction. Figure 2d shows the material stack-up in the \hat{z} -direction. The polarization states of a linearly polarized incident wave with normal and oblique (from -30° to $+30^\circ$ with respect to z -axis) incidence are manipulated as desired after reflected by anisotropic MTS. The key feature of this design is that it allows the conversion of different reflected polarization states such as linear, circular, and cross-polarized waves. Furthermore, the effect of the oblique incident wave with respect to polarization conversion efficiency is also governed by tuning the permittivity of BST film. The present design works for both normal and oblique

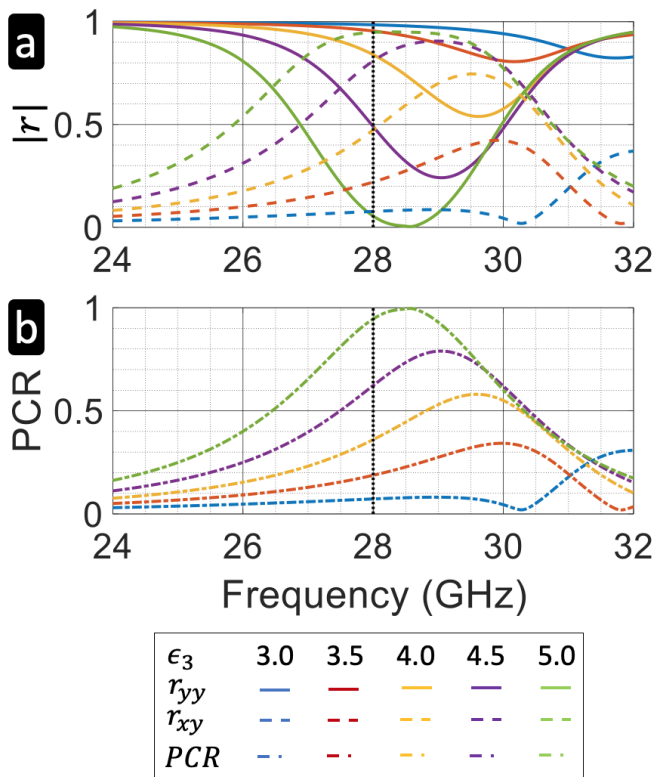


FIG. 3. (a) The reflection coefficient amplitudes $|r|$ and (b) PCR over frequency from $f = 24 - 32$ GHz for our meta-atom in different reconfigurable tuning states as obtained in HFSS EM simulations. The effective dielectric constant for the BST-loaded spacer (ϵ_3) is tuned between the value of 3.0 to 5.0 in steps of 0.5. For $\epsilon_3 = 3.0$, more than 95% of the power from the reflected signal (r_{yy}) is co-polarized with the incident wave from the RF feed. For $\epsilon_3 = 5.0$, more than 95% of the power from the reflected signal (r_{xy}) is converted into the orthogonal cross-polarization. The vertical dotted line denotes the design frequency of $f = 28$ GHz.

(from -30 to $+30^\circ$ with respect to z -axis) incidences. At the operating frequency $f_c = 28$ GHz, the meta-atom has electrical dimension of $\lambda_0/6 \times \lambda_0/6 \times \lambda_0/12$.

We used Ansys HFSS software to perform full-wave EM simulations of our meta-atom design. We also simulated the unit cell in CST Microwave Studio as an additional verification. Figures 2e-f show the surface current distribution for our meta-atom in the co- and cx-polarized states. The bias value of the BST-loaded substrate changes the induced current distribution, resonance, and coupling of our anisotropic meta-atom allowing for polarization rotation. Our MTS rotates polarization of reflected signal from \mathbf{E}_y^r to \mathbf{E}_x^r by tuning ϵ_3 .

The co- and cross-polarized (cx) reflection coefficient magnitudes ($|r|$) and PCR of our reconfigurable polarization meta-atom in different tuning states are shown in Fig. 3. Changing the bias voltage of the tunable BST material reflects a signal with either 90% linear co- or cx-polarized magnitude at $f_c = 28$ GHz depending on the tuning state. We perform polarization modulation us-

ing this tunable mechanism to transmit either a vertical, horizontal, or composite slant polarized signal from the MTS. This MTS design provides a reconfigurable PCR between values of 0.08 to 0.95 (Fig. 3b). This design maintains a PCR greater than 0.9 over a frequency bandwidth (BW) from 27.8 – 29.2 GHz (5.0% BW). If the required tunable PCR range is relaxed, the operational BW is broadened significantly. When $\epsilon_3 = 3.0$, the device maintains a PCR ≤ 0.1 across 24-30.7 GHz.

IV. NUMERICAL EXPERIMENTS

We performed numerical experiments to evaluate the performance of the proposed RMTS-assisted GPSM MIMO system. Throughout the experiments, we use the RMTS Tx, $N_R = 4$, and $K_c = 10$. We employ the maximum likelihood (ML) detector for symbol detection. We analyze the performance by varying N_T , N_{SA} , M , and K with signal-to-noise ratio (SNR) ranging from 0 to 25 dB. In particular, we investigate GPSM cases with $N_{SA} = 1$ or 2. We set

$$\epsilon_k = \begin{cases} \frac{\pi}{4}, & K = 1, \\ \left\{ \frac{\pi}{4}, \frac{\pi}{8} \right\}, & K = 2. \end{cases} \quad (6)$$

Figure 4a compares the BER of GPSM with the conventional MIMO quadrature amplitude modulation (QAM). The RMTS-assisted GPSM performs as well as or better than the traditional MIMO-QAM systems when SE or R are similar. Our numerical experiments show that our RMTS-based GPSM transmitter achieves a 2.7 times lower BER than a traditional MIMO-QAM transmitter at SNR= 15 dB for the same SE and with four times greater EE, since only one subcarrier is used at each signaling interval rather the four. In this example, we utilize only one subcarrier at each signaling interval rather than four simultaneous subcarriers as in MIMO-QAM. The RMTS-based GPSM system uses less activated N_{SA} and RF chains resulting in a superior EE.

We compare the performance of selected GPSM cases when $N_{SA} = 1$ (Fig. 4b) and $N_{SA} = 2$ (Fig. 4c). Our BER results show that an increase in M tends to be more effective than an increase in N_T while keeping other parameters the same. When $N_{SA} = 1$, increasing K from 1 to 2 enhances R by a bit without sacrificing the BER performance (Fig. 4b). The SE is also increased by using $N_{SA} = 2$ with $N_T = 5$ (Fig. 4c). The increased throughput is at the cost of deteriorated BER. By utilizing the polarization states as a DoF, the GPSM system encodes additional information using the polarization states.

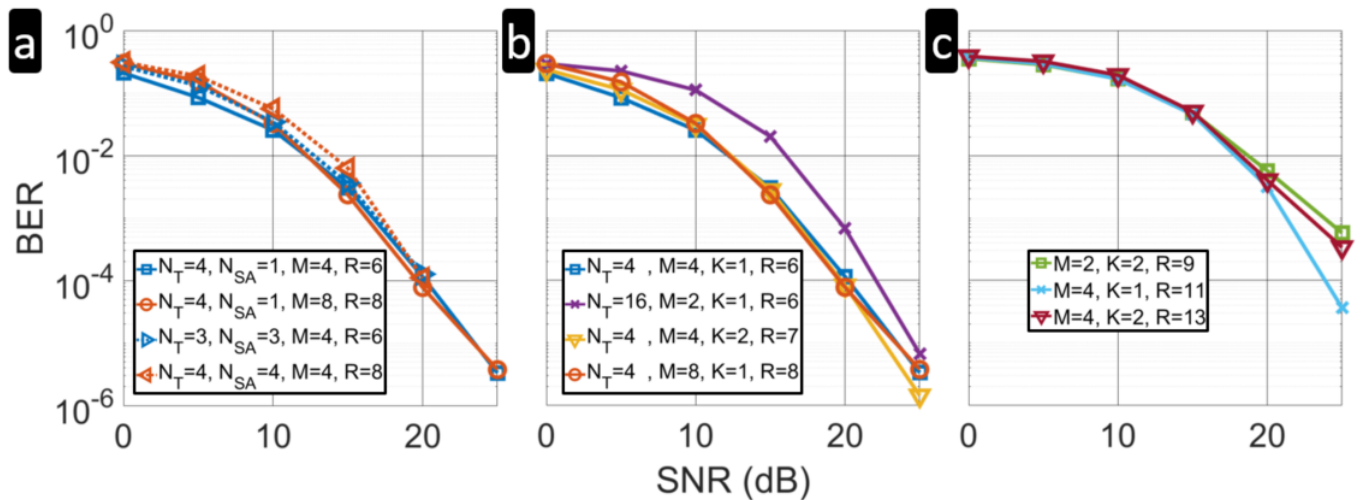


FIG. 4. BER versus SNR for RMTS-assisted GPSM with $N_R = 4$ antennas at the Rx. (a) Performance comparison of GPSM with $K = 1$ (solid lines) and traditional MIMO-QAM (dashed lines) for cases with equal SE. Performance of selected GPSM cases when (b) $N_{SA} = 1$ and (c) $N_{SA} = 2, N_T = 5$. The R is the SE in bits per channel use (bpcu).

V. SUMMARY

We presented RMTS design to simplify wireless communications architectures to support the next-generation IM waveforms that employ polarization as a DoF, such as PolarSK and GPSM. We demonstrated that our BST-based RMTS-assisted GPSM is a promising solution compared to the traditional MIMO-QAM systems when higher SE and EE are required. Our optimized RMTS design provides PCR between values of 0.08 to 0.95 for tunable polarization conversion at 28 GHz. Our numerical simulations show an appreciable BER improvement

of RMTS-based GPSM over conventional MIMO-QAM transmitters at SNR values of ≥ 15 dB and provides four times high EE for the same SE.

ACKNOWLEDGMENTS

J. A. H. acknowledges support from Northrop Grumman Mission Systems (NGMS), Baltimore, MD, for his thesis research. K. V. M. acknowledges support from the National Academies of Sciences, Engineering, and Medicine via Army Research Laboratory Harry Diamond Distinguished Postdoctoral Fellowship.

-
- [1] Q. Qi, X. Chen, L. Lei, C. Zhong, and Z. Zhang, Outage-constrained robust design for sustainable B5G cellular internet of things, *IEEE Transactions on Wireless Communications* **18**, 5780 (2019).
 - [2] N. Ishikawa, S. Sugiura, and L. Hanzo, 50 years of permutation, spatial and index modulation: From classic RF to visible light communications and data storage, *IEEE Communications Surveys & Tutorials* **20**, 1905 (2018).
 - [3] E. Basar, Index modulation techniques for 5G wireless networks, *IEEE Communications Magazine* **54**, 168 (2016).
 - [4] M. Di Renzo, H. Haas, A. Ghayeb, S. Sugiura, and L. Hanzo, Spatial modulation for generalized MIMO: Challenges, opportunities, and implementation, *Proceedings of the IEEE* **102**, 56 (2014).
 - [5] J. Zhang, Y. Wang, J. Zhang, and L. Ding, Polarization shift keying (PolarSK): System scheme and performance analysis, *IEEE Transactions on Vehicular Technology* **66**, 10139 (2017).
 - [6] P. Henarejos and A. I. Pérez-Neira, 3-D polarized modulation: System analysis and performance, *IEEE Transactions on Communications* **66**, 5305 (2018).
 - [7] G. Zafari, M. Koca, and H. Sari, Dual-polarized spatial modulation over correlated fading channels, *IEEE Transactions on Communications* **65**, 1336 (2016).
 - [8] E. Basar, M. Wen, R. Mesleh, M. Di Renzo, Y. Xiao, and H. Haas, Index modulation techniques for next-generation wireless networks, *IEEE Access* **5**, 16693 (2017).
 - [9] J. Zhang, K. J. Kim, A. A. Glazunov, Y. Wang, L. Ding, and J. Zhang, Generalized polarization-space modulation, *IEEE Transactions on Communications* (2019).
 - [10] T. L. Narasimhan, P. Raviteja, and A. Chockalingam, Generalized spatial modulation in large-scale multiuser mimo systems, *IEEE Transactions on Wireless Communications* **14**, 3764 (2015).
 - [11] J. Jeganathan, A. Ghayeb, and L. Szczecinski, Generalized space shift keying modulation for mimo channels, in *IEEE International Symposium on Personal, Indoor and Mobile Radio Communications* (2008) pp. 1–5.
 - [12] J. A. Hodge, K. V. Mishra, and A. I. Zaghoul, Reconfigurable metasurfaces for index modulation in 5G wireless

- communications, in *IEEE International Applied Computational Electromagnetics Society Symposium* (2019) pp. 1–2.
- [13] E. Basar, M. Di Renzo, J. de Rosny, M. Debbah, M.-S. Alouini, and R. Zhang, Wireless communications through reconfigurable intelligent surfaces, *IEEE Access* (2019).
- [14] K. V. Mishra, J. A. Hodge, and A. I. Zaghoul, Reconfigurable metasurfaces for radar and communications systems, in *URSI Asia-Pacific Radio Science Conference* (2019) pp. 1–4.
- [15] E. Basar, Reconfigurable intelligent surface-based index modulation: A new beyond mimo paradigm for 6g, *IEEE Transactions on Communications* **68**, 3187 (2020).
- [16] B. O. Raeker and A. Grbic, Compound metaoptics for amplitude and phase control of wave fronts, *Physical Review Letters* **122**, 113901 (2019).
- [17] C. Pfeiffer and A. Grbic, Metamaterial Huygens' surfaces: Tailoring wave fronts with reflectionless sheets, *Physical Review Letters* **110**, 197401 (2013).
- [18] F. Falcone, T. Lopetegi, M. Laso, J. Baena, J. Bonache, M. Beruete, R. Marqués, F. Martín, and M. Sorolla, Babinet principle applied to the design of metasurfaces and metamaterials, *Physical Review Letters* **93**, 197401 (2004).
- [19] Z. Wu, Y. Ra'di, and A. Grbic, Tunable metasurfaces: A polarization rotator design, *Physical Review X* **9**, 011036 (2019).
- [20] J. Hao, Y. Yuan, L. Ran, T. Jiang, J. A. Kong, C. Chan, and L. Zhou, Manipulating electromagnetic wave polarizations by anisotropic metamaterials, *Physical Review Letters* **99**, 063908 (2007).
- [21] C. Pfeiffer, C. Zhang, V. Ray, L. J. Guo, and A. Grbic, High performance bianisotropic metasurfaces: asymmetric transmission of light, *Physical Review Letters* **113**, 023902 (2014).
- [22] S. Zhang, Y.-S. Park, J. Li, X. Lu, W. Zhang, and X. Zhang, Negative refractive index in chiral metamaterials, *Physical Review Letters* **102**, 023901 (2009).
- [23] H. Kwon, D. Sounas, A. Cordaro, A. Polman, and A. Alù, Nonlocal metasurfaces for optical signal processing, *Physical Review Letters* **121**, 173004 (2018).
- [24] N. I. Landy, S. Sajuyigbe, J. J. Mock, D. R. Smith, and W. J. Padilla, Perfect metamaterial absorber, *Physical Review Letters* **100**, 207402 (2008).
- [25] M. Di Renzo, M. Debbah, D.-T. Phan-Huy, A. Zappone, M.-S. Alouini, C. Yuen, V. Sciancalepore, G. C. Alexandropoulos, J. Hoydis, H. Gacanin, J. de Rosny, A. Bounceur, G. Lerosey, and M. Fink, Smart radio environments empowered by AI reconfigurable meta-surfaces: An idea whose time has come, *EURASIP Journal on Wireless Communications and Networking* **2019**, 129 (2019).
- [26] J. A. Hodge, K. V. Mishra, and A. I. Zaghoul, Multi-discriminator distributed generative model for multi-layer RF metasurface discovery, in *IEEE Global Conference on Signal and Information Processing* (2019) pp. 1–5.
- [27] J. A. Hodge, K. V. Mishra, and A. I. Zaghoul, RF metasurface array design using deep convolutional generative adversarial networks, in *IEEE International Symposium on Phased Array Systems and Technology* (2019) pp. 1–6.
- [28] J. A. Hodge, K. V. Mishra, and A. I. Zaghoul, Joint multi-layer GAN-based design of tensorial RF metasurfaces, in *IEEE International Workshop on Machine Learning for Signal Processing* (2019) pp. 1–6.
- [29] J. A. Hodge, K. V. Mishra, and A. I. Zaghoul, Deep inverse design of reconfigurable metasurfaces for future communications, arXiv preprint arXiv:2101.09131 (2021).
- [30] J. A. Hodge, T. Anthony, and A. I. Zaghoul, Enhancement of the dipole antenna using a capacitively loaded loop (CLL) structure, in *IEEE International Symposium on Antennas and Propagation and USNC-URSI Radio Science Meeting* (2014) pp. 1544–1545.
- [31] J. A. Hodge, T. K. Anthony, and A. I. Zaghoul, Utilizing active circuit elements for dynamic tuning and electronic scanning of CLL-loaded dipole antenna structure, in *USNC-URSI Radio Science Meeting* (2015) p. 16.
- [32] J. A. Hodge, Q. M. Nguyen, and A. I. Zaghoul, Reflective beam steering of metasurface using circular interdigitated self-phased pixels/cells, in *URSI General Assembly and Scientific Symposium* (2020) in press.
- [33] Q. M. Nguyen, J. A. Hodge, and A. I. Zaghoul, Circular inter-digitated design for self-phased reflective pixel/cell for metasurfaces and reflectarrays, in *URSI General Assembly and Scientific Symposium* (2020) in press.
- [34] Q. Nguyen and A. I. Zaghoul, Design of beam steering patch arrays using self-phased metasurface pixels, in *IEEE Antennas and Propagation Society International Symposium* (2020) pp. 1–2.
- [35] J. A. Hodge, K. V. Mishra, and A. I. Zaghoul, Intelligent time-varying metasurface transceiver for index modulation in 6G wireless networks, *IEEE Antennas and Wireless Propagation Letters* **19**, 1891 (2020).
- [36] J. A. Hodge, K. V. Mishra, and A. I. Zaghoul, Media-based modulation with reconfigurable intelligent metasurfaces: Design and performance, in *IEEE International Symposium on Antennas and Propagation and USNC-URSI Radio Science Meeting* (2020) in press.
- [37] N. K. Grady, J. E. Heyes, D. R. Chowdhury, Y. Zeng, M. T. Reiten, A. K. Azad, A. J. Taylor, D. A. Dalvit, and H.-T. Chen, Terahertz metamaterials for linear polarization conversion and anomalous refraction, *Science* **340**, 1304 (2013).
- [38] Y. Z. Cheng, W. Withayachumnan, A. Upadhyay, D. Headland, Y. Nie, R. Z. Gong, M. Bhaskaran, S. Sriram, and D. Abbott, Ultrabroadband reflective polarization convertor for terahertz waves, *Applied Physics Letters* **105**, 181111 (2014).
- [39] C. Fang, Y. Cheng, Z. He, J. Zhao, and R. Gong, Design of a wideband reflective linear polarization converter based on the ladder-shaped structure metasurface, *Optik* **137**, 148 (2017).
- [40] H. F. Ma, G. Z. Wang, G. S. Kong, and T. J. Cui, Broadband circular and linear polarization conversions realized by thin birefringent reflective metasurfaces, *Optical Materials Express* **4**, 1717 (2014).
- [41] H. Yang, X. Cao, F. Yang, J. Gao, S. Xu, M. Li, X. Chen, Y. Zhao, Y. Zheng, and S. Li, A programmable metasurface with dynamic polarization, scattering and focusing control, *Scientific Reports* **6**, 35692 (2016).
- [42] J. Tian, X. Cao, J. Gao, H. Yang, J. Han, H. Yu, S. Wang, R. Jin, and T. Li, A reconfigurable ultra-wideband polarization converter based on metasurface incorporated with PIN diodes, *Journal of Applied Physics* **125**, 135105 (2019).
- [43] Z. Tao, X. Wan, B. C. Pan, and T. J. Cui, Reconfigurable conversions of reflection, transmission, and polarization

- states using active metasurface, *Applied Physics Letters* **110**, 121901 (2017).
- [44] L. Chen, H. L. Ma, Y. Ruan, and H. Y. Cui, Dual-manipulation on wave-front based on reconfigurable water-based metasurface integrated with PIN diodes, *Journal of Applied Physics* **125**, 023107 (2019).
- [45] B. Ratni, A. de Lustrac, G.-P. Piau, and S. N. Burokur, Electronic control of linear-to-circular polarization conversion using a reconfigurable metasurface, *Applied Physics Letters* **111**, 214101 (2017).
- [46] A. Tombak, J.-P. Maria, F. Ayguavives, Z. Jin, G. T. Stauf, A. I. Kingon, and A. Mortazawi, Tunable barium strontium titanate thin film capacitors for rf and microwave applications, *IEEE Microwave and wireless components letters* **12**, 3 (2002).
- [47] S. J. Orfanidis, *Electromagnetic waves and antennas* (Rutgers University New Brunswick, NJ, 2002).

SUPPLEMENT: SIGNAL MODEL

Consider a RMTS-enhanced GPSM transmitter for a generic DP-MIMO system with N_T Tx and N_R Rx antennas. The RMTS is partitioned into N_{SA} SAs connected to $N_{RF} = 1$ RF chain. The transmitter employs a size- P polarization constellation of $N_{SA} \times 1$ vectors $\mathbf{x}_0, \mathbf{x}_1, \dots, \mathbf{x}_p, \dots, \mathbf{x}_{p-1}$, each with an average symbol power $E[|\mathbf{x}_p|^2] = 1$. We represent the polarization state of $\mathbf{x}_{p,n_{SA}}$ - the n_{SA} -th element of \mathbf{x}_p - using Jones vector in a right-handed Cartesian coordinate system [5, 9] as

$$\mathbf{x}_{p,n_{SA}} = \frac{1}{\sqrt{N_{SA}}} \begin{bmatrix} x_{p,n_{SA},V} \\ x_{p,n_{SA},H} \end{bmatrix}, \quad (7)$$

where

$$x_{p,n_{SA},V} = \cos \epsilon_{k,n_{SA}} \exp\left(j2\pi \frac{m_{V,n_{SA}} - 1}{M}\right), \quad (8)$$

$$x_{p,n_{SA},H} = \sin \epsilon_{k,n_{SA}} \exp\left(j2\pi \frac{m_{H,n_{SA}} - 1}{M}\right), \quad (9)$$

are the signals transmitted by vertically and horizontally polarized transmit antennas, respectively; $\epsilon_{k,n_{SA}}$ denotes the polarization angle with $k = 1, 2, \dots, K$; and $m_{V,n_{SA}}, m_{H,n_{SA}} = 1, 2, \dots, M$ are the phase indices of the respective signals reflected by the n_{SA} -th SA. The set $\{M, K\}$ determines the size of the GPSM signal constellation so that $P = M^2 K$. The signals with linear, circular or elliptic polarization states are determined by the parameter set $\{m_{V,n_{SA}}, m_{H,n_{SA}}, k\}$. They are generated by each activated DP transmit SA according to (7). For each transmission, N_{SA} sets of $\{k, x_{p,n_{SA},V}, x_{p,n_{SA},H}\}$ are selected to convey $N_{SA} \log_2(M^2 K)$ information bits.

Define the $N_{SA} \times 1$ vectors of the meta-atom reflection parameters $\boldsymbol{\theta}_{V,H} = [\theta_{1,V,H}, \dots, \theta_{N_{SA},V,H}]^T$ and $\boldsymbol{\beta} = [\beta_{1,V,H}, \dots, \beta_{N_{SA},V,H}]^T$, where $\theta_{n,V,H} \in [0, 2\pi)$ and $\beta_{n,V,H} \in [0, 1]$ denote the phase shift and the amplitude reflection coefficient for the V and H polarization components of the n -th SA of the RMTS, respectively; and $(\cdot)^T$ denotes the vector transpose. The $N_{SA} \times N_{SA}$ RMTS reflection-coefficient diagonal matrix is $\boldsymbol{\Theta}_{V,H} = \text{diag}(\boldsymbol{\beta} \odot \exp[j\boldsymbol{\theta}]) = \text{diag}(\beta_{1,V,H} e^{j\theta_{1,V,H}}, \dots, \beta_{N_{SA},V,H} e^{j\theta_{N_{SA},V,H}})$, where \odot denotes the Hadamard product. By changing the bias voltage to each meta-atom of the RMTS, we tune $\theta_{n,V,H}$ and $\beta_{n,V,H}$ such that $\theta_{n_{SA},V,H} = \left(2\pi \frac{-1+m_{V,H,n_{SA}}}{M}\right)$ to realize the polarization modulation states for $\mathbf{x}_{p,n_{SA}}$.

The $2N_T \times 1$ transmitted symbol vector is $\mathbf{s} = [\mathbf{s}_1^T, \dots, \mathbf{s}_{n_T}^T, \dots, \mathbf{s}_{N_T}^T]^T$ where the modulated signal \mathbf{s}_{n_T} is a two-element vector transmitted over the n_T -th dual-polarized SA antenna. The signals transmitted by N_{SA} activated transmit SAs are denoted by the vector $\mathbf{x} = [\mathbf{x}_{p,1}^T, \dots, \mathbf{x}_{p,n_{SA}}^T, \dots, \mathbf{x}_{p,N_{SA}}^T]^T$. Note that \mathbf{x} is a decimation of non-zero elements in \mathbf{s} because $N_T > N_{SA}$. The conversion from low-dimension symbol vector \mathbf{x} to high-dimension transmit signal \mathbf{s} is achieved through a

$2N_T \times N_{SA}$ index mapping matrix \mathbf{U} . Define $\mathcal{T} \subseteq \{1, 2, \dots, 2N_T\}$ be the index set with $|\mathcal{T}| = N_{SA}$. Then, the n th row of matrix \mathbf{U} is

$$[\mathbf{U}]_n = \begin{cases} \mathbf{0}_{N_{SA}}^T, & n \notin \mathcal{T}, \\ \mathbf{1}_{N_{SA}}^T, & n \in \mathcal{T}, \end{cases} \quad (10)$$

where $\mathbf{0}_{N_{SA}}$ and $\mathbf{1}_{N_{SA}}$ denote $N_{SA} \times 1$ all-zeroes and all-ones vectors, respectively. Consequently, $\mathbf{s} = \mathbf{U}\boldsymbol{\Theta}_{V,H}\mathbf{x}$.

Denote the polarization dependent channel path $\mathbf{H}_{n_R,n_T} \in \mathbb{C}^{2 \times 2}$ between each Tx subarray and receiver (Rx) pair as

$$\mathbf{H}_{n_R,n_T} = \begin{bmatrix} h_{VV,n_R,n_T} & h_{VH,n_R,n_T} \sqrt{\chi} \\ h_{HV,n_R,n_T} \sqrt{\chi} & h_{HH,n_R,n_T} \end{bmatrix}, \quad (11)$$

where χ denotes the expected power ratio of co-polarized channel to cross-polarized channel and each element denotes the channel gain from the n_T -th DP antenna at the transmitter of a particular polarization (H or V) to the n_R -th DP antenna at the Rx; the first polarization subscript corresponds to Tx. We determine the value of χ through full-wave EM simulation (as shown in Fig. 3). Then, the $2N_R \times 2N_T$ channel matrix \mathbf{H} in terms of Tx subarray and Rx pairs \mathbf{H}_{n_R,n_T} is

$$\mathbf{H} = \begin{bmatrix} \mathbf{H}_{1,1} & \mathbf{H}_{1,2} & \cdots & \mathbf{H}_{1,N_T} \\ \mathbf{H}_{2,1} & \mathbf{H}_{2,2} & \cdots & \mathbf{H}_{2,N_T} \\ \vdots & \vdots & \ddots & \vdots \\ \mathbf{H}_{N_R,1} & \mathbf{H}_{N_R,2} & \cdots & \mathbf{H}_{N_R,N_T} \end{bmatrix}. \quad (12)$$

For line-of-sight (LoS) wireless communications, the standard statistical model for a multipath fading channel follows a Rician distribution. Here, the $N_R \times N_T$ complex channel impulse response (CIR) \mathbf{H} is modeled as the sum of the fixed LoS component and a random multipath non-LoS (nLoS) channel component as

$$\mathbf{H} = \sqrt{\frac{K_c}{K_c + 1}} \mathbf{H}_L + \sqrt{\frac{1}{K_c + 1}} \mathbf{H}_N, \quad (13)$$

where K_c is the real-valued Rician K -factor of the channel, $\mathbf{H}_L \in \mathbb{C}^{N_R \times N_T}$ is the LoS channel component that remains unchanged during the channel coherence time, and $\mathbf{H}_N \in \mathbb{C}^{N_R \times N_T}$ is the nLoS fading component representing random multipath fading.

The Rician K_c -factor is the power ratio of direct path (LoS) to other scattered nLoS paths. For a narrow-band block-fading channel, the received signal is

$$\mathbf{y} = \mathbf{H}\mathbf{s} + \mathbf{n}, \quad (14)$$

where $\mathbf{y} \in \mathbb{C}^{2N_R \times 1}$ is the output of N_R Rx antennas, $\mathbf{s} \in \mathbb{C}^{2N_T \times 1}$ are the transmit symbols from N_T dual-polarized transmit antennas, and $\mathbf{n} \in \mathbb{C}^{2N_R \times 1}$ is the circularly symmetric additive white Gaussian noise.

The RMTS aperture dynamically reconfigures N_T by splitting it into multiple SAs. In full-aperture configuration, $N_{SA} = N_T = 1$. Given the RMTS aperture area A and the operating wavelength λ , the full-aperture results

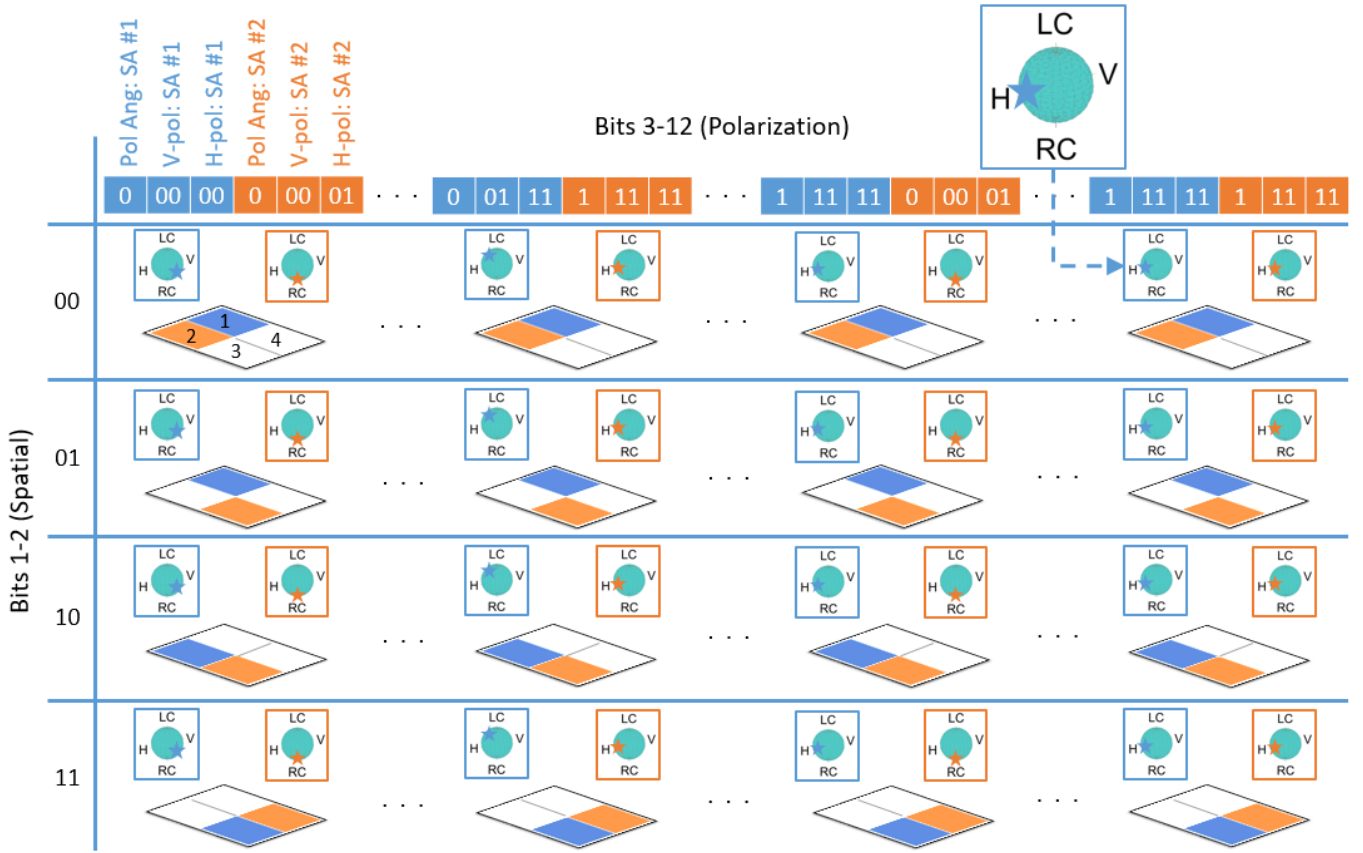


FIG. 5. Illustration of mapping a 12-bit sequence to subarrays and polarization states in an RMTS-enhanced GPSM transmitter with data rate of $R = 12$ bits/s/Hz. Here, $N_T = 4$, $N_{SA} = 2$, $K = 2$, and $M = 4$. On the vertical axis, bits 1-2 are spatial selector bits that determine the activated SAs. The colored elements are set to be active based on index bits. The indices of the SAs are labeled as 1 to N_T (upper left). On the horizontal axis, bits 3-7 (blue) and 8-12 (orange) determine the polarization states for the first and second activated SAs, respectively. The polarization of each transmit signal follows (9) and is represented on the Poincaré sphere (top right).

in higher aperture directivity $D \approx 4\pi A/\lambda^2$, increased Tx antenna gain and improved Rx SNR.

When RMTS is configured as multiple sub-apertures (e.g. $N_{SA} = 2$ or 4), the data rate is increased by operating as a MIMO Tx at the expense of lower aperture directivity and gain (arising from reduced radiating area of each subarray as A/N_{SA}).

For each transmission, the selections of polarization state and activated transmit DP antennas convey $N_{SA} \lceil \log_2(M^2 K) \rceil$ and $L = \lceil \log_2 \left(\frac{N_T}{N_{SA}} \right) \rceil$ bits, respectively. The resulting SE is

$$R = \left\lceil \log_2 \left(\frac{N_T}{N_{SA}} \right) \right\rceil + N_{SA} \lceil \log_2(M^2 K) \rceil \text{ bits/s/Hz.} \quad (15)$$

This is similar to conventional GPSM but no longer restricted by the physical N_{RF} (see Table I). At the Rx, the indices of combination of activated transmit antennas and transmit polarization state is determined for signal detection. After decoding the received symbols through, for example, the ML detector [3], BER is computed.

Figure 5 shows the index mapping procedure for this RMTS-enhanced GPSM transmitter. Data bits are divided into spatial- and polarization-signaling bits which determine the activated SAs and the transmit wave's polarization for each SA defined by (7)-(9). Denote the number of spatial-signaling bits by q . Then, the number of combinations of N_{SA} transmitters that are selected by q bits are $2^q = Q \leq \binom{N_T}{N_{SA}}$. Denote the set of all Q combinations of subarrays by \mathcal{S} , $|\mathcal{S}| = Q$. A bijective map $g : \{0,1\}^q \rightarrow \mathcal{S}$ maps the q bits of the codeword to activated subarrays in the set \mathcal{S} . For example, when $q = 2$, $N_{SA} = 2$, $N_T = 4$ with each transmitter indexed by an element of the set $\{1, 2, 3, 4\}$, and $\mathcal{S} = \{(1, 2), (1, 3), (2, 3), (3, 4)\}$, a possible mapping of spatial bits to activated SAs is

$$\underbrace{\{00, 01, 10, 11\}}_{\text{Spatial bits}} \xrightarrow{g(\cdot)} \underbrace{\{(1, 2), (1, 3), (2, 3), (3, 4)\}}_{\text{Active SAs}}.$$